Energy and AI 10 (2022) 100188

Contents lists available at ScienceDirect

Energy and AI

journal homepage: www.sciencedirect.com/journal/energy-and-ai

Battery state-of-charge estimation using machine learning analysis of ultrasonic signatures

Elias Galiounas [a,b,c], Tom G. Tranter [a,b,*], Rhodri E. Owen [a,b], James B. Robinson [a,b], Paul R. Shearing [a,b], Dan J.L. Brett [a,b,*]

[a] Electrochemical Innovation Lab, Department of Chemical Engineering, University College London, London, WC1E 7JE, UK
[b] The Faraday Institution, Quad One, Becquerel Avenue, Harwell Campus, Didcot, OX11
[c] The Alan Turing Institute, British Library, 96 Euston Road, London NW1 2DB

HIGHLIGHTS

- Reflected ultrasonic signals from battery internal structures show high correlation with the state-of-charge.
- Holistic treatment of acoustic waveforms using deep learning removes reliance on specific waveform peaks.
- Feature selection based on Pearson statistical correlation can provide both accuracy and computational improvements.
- Utilisation of the frequency domain for State-of-Charge inference and neural network training maximises the estimation accuracy.

GRAPHICAL ABSTRACT

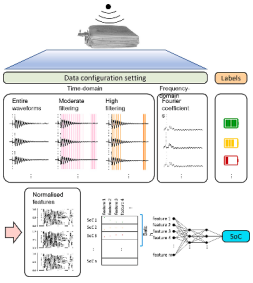

ARTICLE INFO

Keywords:
Battery diagnostics
Ultrasonic battery monitoring
Acoustic battery inspection
Mechanical-electrochemical correlation
Machine learning
Artificial neural networks

ABSTRACT

The potential of acoustic signatures to be used for State-of-Charge (SoC) estimation is demonstrated using artificial neural network regression models. This approach represents a streamlined method of processing the entire acoustic waveform instead of performing manual, and often arbitrary, waveform peak selection. For applications where computational economy is prioritised, simple metrics of statistical significance are used to formally identify the most informative waveform features. These alone can be exploited for SoC inference. It is further shown that signal portions representing both early and late interfacial reflections can correlate highly with the SoC and be of predictive value, challenging the more common peak selection methods which focus on the latter. Although later echoes represent greater through-thickness coverage, and are intuitively more information-rich, their presence is not guaranteed. Holistic waveform treatment offers a more robust approach to correlating acoustic signatures to electrochemical states. It is further demonstrated that transformation into the frequency domain can reduce the dimensionality of the problem significantly, while also improving the estimation accuracy. Most importantly, it is shown that acoustic signatures can be used as sole model inputs to produce highly accurate SoC estimates, without any complementary voltage information. This makes the method suitable for applications where redundancy and diversification of SoC estimation approaches is needed. Data is obtained experimentally from a 210 mAh $LiCoO_2$/graphite pouch cell. Mean estimation errors as low as 0.75% are achieved on a SoC scale of 0–100%.

* Corresponding authors.
E-mail addresses: t.tranter@ucl.ac.uk (T.G. Tranter), d.brett@ucl.ac.uk (D.J.L. Brett).

https://doi.org/10.1016/j.egyai.2022.100188

Available online 23 July 2022

1. Introduction

Estimating the State-of-Charge (SoC) of batteries is a non-trivial task of inference rather than direct measurement. In the majority of applications today, batteries are observed externally via voltage and current measurements at the battery terminals together with temperature monitoring. These signals can be utilised for SoC estimation using a range of existing methods, as outlined in recent reviews [1–4].

A popular and simple technique is coulomb counting, which is the integration of current flows through the battery over time. Although straightforward, coulomb counting is rarely used in isolation due its sensitivity to initialisation and its propensity to accumulate measurement error [5,6]. Another popular method is the mapping of the Open-Circuit-Voltage (OCV) to the SoC using look-up tables constructed from experiments [7]. In the case of lithium-ion batteries such mappings exploit the monotonic dependence of the OCV to the SoC [8,9], however, the cell must be in a state of equilibrium when measurements are taken. This is rarely practical. Additionally, certain lithium-ion chemistries such as Lithium-Iron-Phosphate (LFP) have very flat OCV curves [10] leading to poor accuracy in the mapping. In chemistries beyond lithium-ion, the SoC—OCV relationship is not even necessarily monotonic [11].

A more comprehensive approach is to account for cell dynamics in the SoC estimation by employing a model of the cell. Models can be constructed in four major ways. Physics-Based-Models attempt to capture the main electrochemical reactions from first principles, and require extensive testing of constituent cell components to be parameterised [12,13]. Alternatively, models which assume simpler equations-of-state can be constructed, capturing only the behavioural characteristics of interest. These primarily take the form of Equivalent-Circuit-Models (ECMs) [14,15] with linear circuit components, or in combination with impedance-specific components [16,17]. ECMs have tunable parameters which can be calibrated based on full-cell testing. More abstractly than ECMs, data driven models can learn the equations-of-state from operating data, or dynamic tests, using techniques from the field of machine learning [18,19]. Hybrid approaches also exist, combining elements of the above [20,21].

The link between battery models and SoC estimation is usually achieved using observer algorithms. The Extended Kalman filter [22–24], and its many variants [25–30], is the workhorse of observer implementations for SoC estimation. Deep Neural Networks have shown great success when employed together with observer algorithms [31,32], or also independently [33–35]. Recurrent Neural Networks in particular are able to consider a time-series of measurements in the estimation, therefore accounting for cell dynamics without the need for an observer algorithm [36–40].

Although the above methods have been largely adequate for most systems, they all rely on the external measurements of voltage, current and temperature. As cells with increased energy content are being deployed, the ability to estimate SoC with redundancy is becoming safety-critical. Ultrasonic monitoring offers a new method of inferring the SoC using an independent signal, which contains rich insights from the internal structure of a cell and is suitable for rapid data acquisition. These attributes also make the ultrasonic method suitable for a data-driven implementation as will be shown.

Ultrasonic waves are widely used in multiple fields of engineering, science and medicine, for the visualisation and inspection of sub-surface structures. In recent years, the ultrasonic method has found applications in the study of a broad range of electrochemical power systems, as outlined in the review of Majasan et al. [41]. In principle, any form of ultrasonic inspection begins with the pulsing of mechanical stress waves through a volume of material, which are then influenced by variations in the material properties and the presence of interfaces. As a result, acoustic signals with a history of travel can be very informative, and methodologies to extract the information carried by them are continuously being developed [42–46].

Ultrasonic waves can be grouped into two categories; body (or bulk) waves and surface (or guided) waves [41]. The optimality of either type for the study of batteries is a topic of debate [47,48]. In the simplest possible setup, the ultrasonic technique employs a pulser-receiver device, together with a single piezoelectric transducer operating in pulse-echo mode. The pulser-receiver periodically produces electrical impulses, causing the transducer to vibrate and transmit a mechanical stress wave through the battery. The same transducer then senses echoes of the signal, as the wave is reflected at battery interfaces or the posterior battery surface. Reflections are recorded by the pulser-receiver in the form of waveforms, which are finite time series of the acoustic intensity. Instead of monitoring pulse echoes, or in addition to it, it is also possible to monitor the transmitted signal by using a second transducer operating in receive mode on the posterior side of the cell. More than two transducers can also be employed to study multiple transmission paths [49]. Most often ultrasonic inspection is applied to pouch cells which, due to their flat form, lend themselves to ultrasonic testing with flat-head transducers [47–59] . A smaller number of studies on cylindrical cells can be found in the literature [60].

Hsieh et al. [60] and Sood et al. [61] were amongst the first to explore, qualitatively, the correlation between the acoustic signatures of cells and their SoC and State-of-Health (SoH). Hsieh et al. employed both acoustic modelling and experiments to observe how acoustic waveforms were altered by state changes. They considered both transmitted and reflected signals and focused their observations on the Time-of-Flight (ToF) of selected waveform peaks and their respective acoustic intensity. The general trend seen in their study is that as the SoC increases, ToF shifts to lower values because the acoustic waves traverse the cells more quickly. Acoustic intensity, on the other hand increases. This observation was made using body waves, while the same is noted by Ladpli *et al.* [47] who employ guided waves. It should be emphasised that these trends are not linear or strictly monotonic in either study. Robinson et al. [50] and Popp et al. [62] also point to non-linearities in the acoustic response of cells with $LiCoO_2$ (LCO) and nickel-manganese-cobalt (NMC) cathodes, respectively. As will be discussed, artificial neural networks show great success at modelling the non-linear nature of the correlation between acoustic signatures and the SoC.

To understand and justify the decrease in the ToF with increasing SoC, two conflicting mechanisms must be considered. One is the change in the cell thickness with SoC, and the other is the change in the acoustic velocity, as influenced by alterations in the material properties of the electrodes. The dependence of the ToF on these parameters is approximated by Eqn. (1), where E and ρ are the aggregate Young's Modulus and density, and L is the cell thickness [51,60].

$$ToF = \frac{L}{\sqrt{E/\rho}} \tag{1}$$

A typical lithium-ion cell stack expands in thickness during charge, partly due to the lithiation of the graphite anode causing a ~10% volume increase compared to its fully delithiated state [58]. In the case of LCO cathodes, it is reported that simultaneous expansion takes place upon delithiation, resulting in both electrodes expanding as the cell charges [63]. Thickness changes alone would lead to a longer ToF at higher SoCs. Since the opposite is observed in multiple studies [51,59], it is inferred that the change in material properties results in the speed of sound increasing with SoC, outweighing the thickness increase. Therefore, it appears that in a typical cell the net modulus-to-density ratio of the combined anode and cathode increases with SoC, disregarding current collectors and separators which should remain largely unaffected. Other negative electrode materials may shift this balance, such as silicon, which is reported to expand by up to 300% when highly lithiated [64]. When testing NMC/graphite cells, it has been reported that the cathode modulus and density generally decrease with SoC, but the anode modulus and density both increase [47]. Focusing on graphite

anodes alone, a roughly three-fold increase in modulus has been shown to take place with full lithiation compared to zero lithiation [58]. It is this 'stiffening' of the anode which seems to dominate the acoustic ToF response.

The correlation between acoustic attenuation and SoC is less well understood. Ladpli et al. [47] hypothesise that acoustic attenuation is governed by changes in the viscoelastic properties of the cell. They argue that a more rigid material tends to be less dampening to acoustic waves, causing intrinsically less attenuation. Therefore, they attribute the stronger signal intensity they observe at higher SoC to the enhanced modulus at those states. A similar argument is put forward by Chang et al. [58]. On the other hand, Gold et al. [53] perform an acoustic frequency scan which demonstrates that acoustic attenuation in batteries increases dramatically when the actuation wavelengths are close to the electrode layer thickness. They attribute this effect to enhanced dispersion at the layer boundaries.

A number of attempts to quantitatively link SoC and SoH to acoustic measurements are found in the literature. The majority of them utilise the time-domain form of recorded signals and perform some type of acoustic peak selection in their workflows [47,53,55]. A smaller number of studies attempt to extract insights from the frequency domain [48,49]. Davies et al. [55] employ Support Vector Regression to estimate SoC and SoH using ultrasonic measurements in a supervised machine learning routine. They reduce the ultrasonic waveform to two key metrics, the ToF shift against a reference signal, and what they refer to as 'total signal amplitude'. To compute the ToF shift of a signal against a reference they calculate the cross-correlation of the two, and the shift is obtained using the point of best correlation. It can therefore be argued that this type of ToF shift computation is representative of the entire signal and not any specific peak or position. The 'total amplitude' is calculated as the integral of the acoustic intensity over the full waveform; therefore, it is a measure of signal energy. This treatment of the amplitude also implicitly contains information from the signal as a whole. To perform SoC estimation the authors use their two acoustic metrics, with the inclusion of cell voltage for better accuracy. For the estimation of SoH, they use both acoustic metrics together with the voltage and the complete acoustic waveform.

Gold et al. [53] use body waves to probe cells at relatively low frequencies, in the vicinity of 200 kHz compared to the more common 2.5–5 MHz seen in other body wave studies [60,61,65]. The authors argue that such a frequency provides the conditions for two separate compressional waves to be energised within the cell, as predicted by Biot's theory of elastic wave propagation in fluid-saturated porous media [66,67]. The authors detect both waves in acoustic transmission mode and proceed to identify their respective peaks using a windowed local maximum search on the signal amplitude. They compute the signal amplitudes of those characteristic peaks and examine their correlation to the SoC. They observe that the faster wave exhibits no correlation, whereas the slower wave does. They use the latter to perform linear regression to estimate the SoC. It is worth noting that the authors attempt to train SoC estimators using acoustic information alone, similar to the present study, without any assistive voltage measurements.

Ladpli et al. [47] use four transducers in a network configuration, operated in pitch-catch mode to record transmitted signals. Instead of using step pulse actuation, they probe their cells with wave packets that are five-peak Hanning-windowed tone bursts. Their analysis also focuses on two fundamental time-domain parameters, the signal amplitude and the ToF. Signal amplitude is computed as the maximum amplitude of the sensing signal's Hilbert Envelope and the ToF is calculated as the time taken by an actuation wave packet as a whole to reach a sensor. The authors assess the predictability of SoC and SoH from their acoustic dataset using Generalised Additive Models, a semi-parametric regression technique that allows dependant variables to be described by smooth non-linear functions of covariates. They statistically examine different sets of covariates, including combinations of ToF and signal amplitudes from different transducer pairs and quote a good overall predictive capability. Notably, voltage is not used as a covariate in their study, which focuses on acoustic characteristics in isolation.

Copley et al. [48] argue that any reliance on specific acoustic peaks, or peak envelopes, to perform inference should be avoided. By developing an acoustic model based on the 1D wave equation they demonstrate that certain material layer combinations can make it very difficult to identify any form of peak in the recorded signals from which to take measurements. To alleviate this difficulty, they propose a methodology to automatically identify the best waveform location for SoC correlation, which invokes the frequency domain via the Cross-Wavelet Transform (XWT). They propose that the XWT is advantageous compared to the more conventional Fast Fourier Transform (FFT) because it maintains information from both the time and the frequency domains when monitoring signal changes. The FFT, on the contrary, would discard all time-domain information. Nevertheless, in their study the authors isolate a single frequency from the XWT spectrum, specifically the actuation frequency of their experiment, and monitor the transformed intensity for that frequency in time. They further apply arbitrary scaling based on the phase shift, and a weighting to favour later ToFs which they believe to be more information-rich. Even though it is intuitive that signal portions originating at distant battery locations may accumulate greater state insights by the time they reach the transducer, the presence of obstacles such as tabs or delamination pockets can render them elusive. Over-reliance on them is, therefore, discouraged.

A more straightforward examination of the frequency domain is performed by Chang et al. [58], although their study is mostly observational and no SoC or SoH predictors are trained. Similar to Robinson et al. [54] they develop 2D scanning modalities to observe spatial acoustic characteristics of cells, but this time also in the frequency domain which is obtained via FFT of the recorded waveforms. Importantly, by producing spatially-resolved 'heatmaps' of the acoustic responses in both the time- and frequency-domain, they observe that frequency-domain methods can reveal spatial and temporal variations that are not apparent in the time-domain. The authors argue that the frequency response may show greater sensitivity to conditions such as uneven cell wetting compared to time-domain analysis. It should be noted that amongst the entire frequency spectrum they choose to observe a narrow frequency band in the vicinity of 1 MHz. Interestingly, this is not the actuation frequency of their experiment, but is instead chosen based on having the largest Fourier coefficient magnitude.

Features informed by both time and frequency characteristics are extracted from guided wave signals in [49] using a matching pursuit time-frequency representation [68]. In essence, the authors decompose their recorded signals into a linear combination of 10 constituent waveforms, selected from the Gabor dictionary which contains standardised scaled, translated, and modulated versions of windowed tone bursts similar to their actuation signal. Their matching pursuit algorithm estimates a set of possible Gabor parameters, which are coefficients of scaling, translation, modulation, and phase change. Following additional processing, the Gabor parameters are used as predictive features which correlate to SoC and SoH.

In this work, artificial neural networks are explored to link acoustic signatures to the SoC of a cycling pouch cell for SoC estimation. The processing of entire waveforms is demonstrated, without any prior feature selection, creating streamlined workflows of regression model training and evaluation. Being cognisant of the motivations around feature selection and dimensionality reduction in the regression process, it is also shown that a simple feature filtering process based on statistical significance can be applied, yielding comparable or better SoC predictions to the full waveform case. Statistical significance is quantified using the Pearson correlation coefficient between any feature and the SoC. The use of Fourier coefficients from a frequency domain subset is also explored, and their predictive value as regression features is evaluated in comparison to the time-domain.

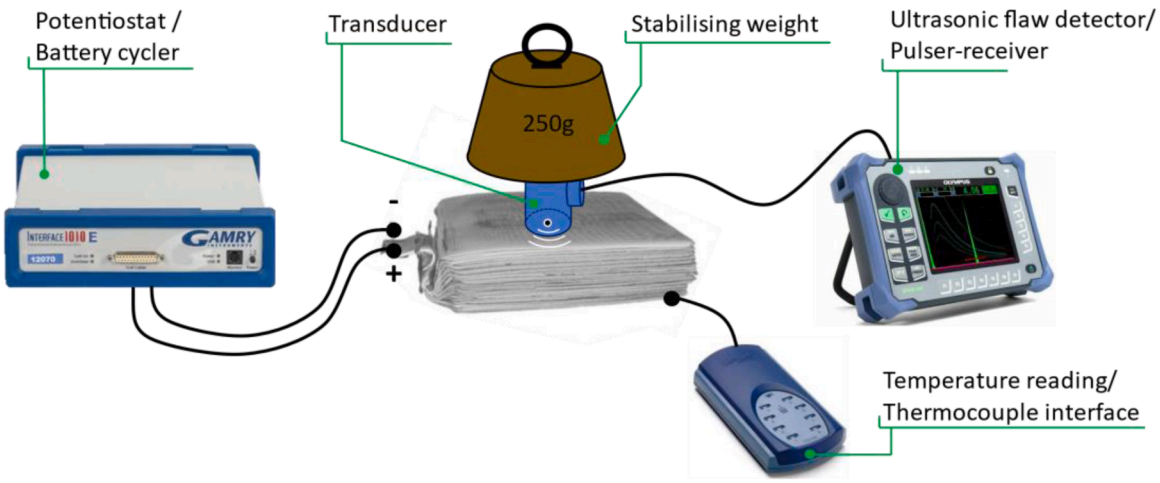

Fig. 1. Acoustic testing setup.

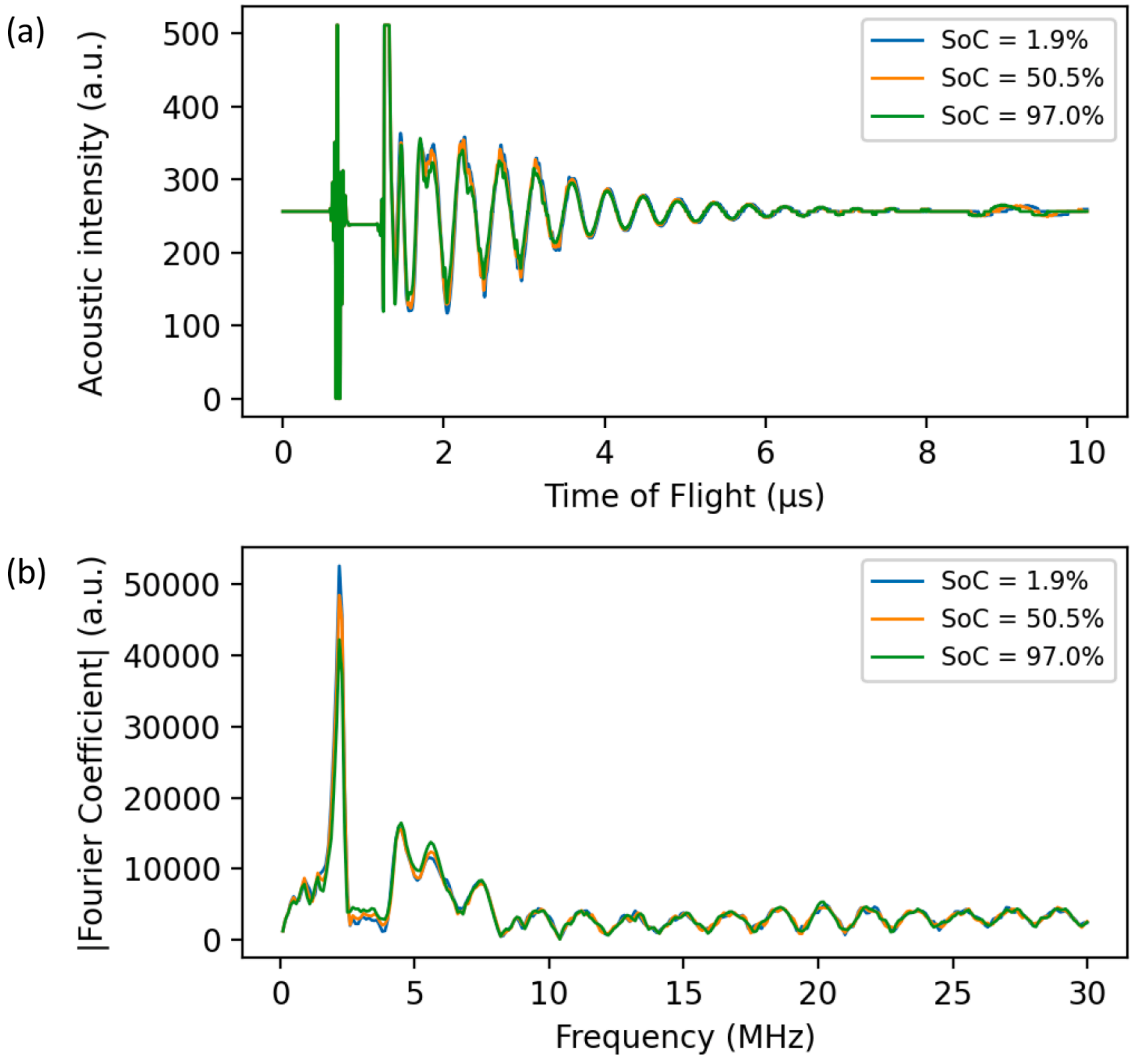

Fig. 2. Example signals from the bottom, middle and top of the SoC range. All signals are from the 1st charge cycle at C/5. (a) Time-domain representation. (b) Frequency domain representation cropped to the 15% lowest frequencies.

Table 1
Data configurations.

Time-domain data configurations	1	All 4000 features.
	2	995 features selected based on having an absolute Pearson correlation coefficient to SoC greater than 0.5.
	3	361 features selected based on having an absolute Pearson correlation coefficient to SoC greater than 0.75.
Frequency-domain data configuration	1	Fourier coefficient magnitudes of the lowest 300 frequencies.

2. Methodology

2.1. Experimental methods

The dataset used in this work was obtained in an earlier study [69], using the following setup and materials. A commercial 210 mAh lithium-ion pouch cell composed of an LCO cathode and a graphite anode (PL-651,628–2C, AA Portable Power Corp., Richmond, CA, USA) with stacked electrode layers was tested with the ultrasonic setup shown in Fig. 1. The same cell was previously considered in several other studies [52,55,57,59]. Acoustic measurements were taken with the cell cycling between 2.75 and 4.2 V using a CC-CV protocol. Five cycles were performed at each of the rates C/5, C/2 and 1C, in this order, with a C/20 cut-off current at the top of charge during the CV step. The acoustic equipment comprised an Epoch 650 ultrasonic flaw detector (Olympus Corp., Japan) and a 6 mm diameter transducer with a centre frequency of 5 MHz (M110-RM, Olympus Corp. Japan). The transducer was operated in pulse-echo mode and acoustic gel couplant (type H-2, Olympus Corp. Japan) was applied between the transducer and the cell. A 250 g weight was placed on top of the transducer to ensure consistent contact throughout the experiment, secured in place by a custom designed 3D printed holder. Cycling was performed using an Interface 1010E potentiostat (Gamry Instruments, U.S.A.). Actuation pulse signals were produced with an energy setting of 300 V, received signals were recorded over a time range of 10 μs after pulsing and were amplified with a gain of 60 dB. Acoustic measurements were taken approximately every 60 s. Experiments were conducted at ambient laboratory conditions. The temperature of the cell was monitored using a K-type thermocouple on the surface of the cell and a TC-08 thermocouple interface (PicoTech, U.K.). The cell temperature was found to vary between 24.9 and 29.9°C (mean: 26.0°C, standard deviation: 0.6°C). The SoC was calculated by 'Coulomb counting' using the cycling data records.

2.2. Computational methods

A total of 5045 waveform samples were recorded during the experiment. Each waveform captures 10 μs of sound travel and comprises 4000 equidistant data points in the time domain. Waveforms were also transformed to the frequency domain using FFT, where intrinsically the number of datapoints was reduced from 4000 to 2000, discarding negative frequencies which yield equal Fourier coefficients to their positive counterparts. A further reduction was applied to the frequency domain, maintaining only the Fourier coefficients of the lowest 300 frequencies (first 15%). This threshold is arbitrary and assumes that the signal-to-noise ratio diminishes at higher frequencies. Time-domain and frequency-domain signals corresponding to three example SoCs are plotted in Fig. 2. Individual data points in each domain were treated as predictive features and were used in the data configurations listed in Table 1 to perform regression analysis estimating the SoC over its full range (0% to 100%).

The Pearson correlation coefficient was used as an indicator of statistical significance to perform feature selection in the time-domain, producing data configurations 2 and 3. It is a normalised measurement of the covariance of each waveform feature and the SoC corresponding to that waveform (Eqn. (2)). It obtains values in the range −1 to 1, with the extremities indicating a perfectly linear correlation and zero indicating no correlation. A time-domain envelope of all recorded waveforms is shown in Fig. 3 together with the absolute Pearson correlation for all features, highlighting the correlation bands that were used for feature selection. A complementary view of the acoustic envelope and unbanded Pearson correlation is given in supplementary Figure S1.

$$\text{Pearson correlation} = \frac{\sum (x - m_x)(\text{SoC} - m_{\text{SoC}})}{\sqrt{\sum (x - m_x)^2 \sum (\text{SoC} - m_{\text{SoC}})^2}} \quad (2)$$

x Intensity of acoustic feature

m_x Mean of feature vector x (across all waveform samples)

SoC State of Charge corresponding to the x value (and the waveform it belongs to)

m_{SoC} Mean SoC recorded in the experiment

The correlation between time-domain or frequency-domain features and the SoC can also be observed in the normalised colourmaps of Fig. 4,

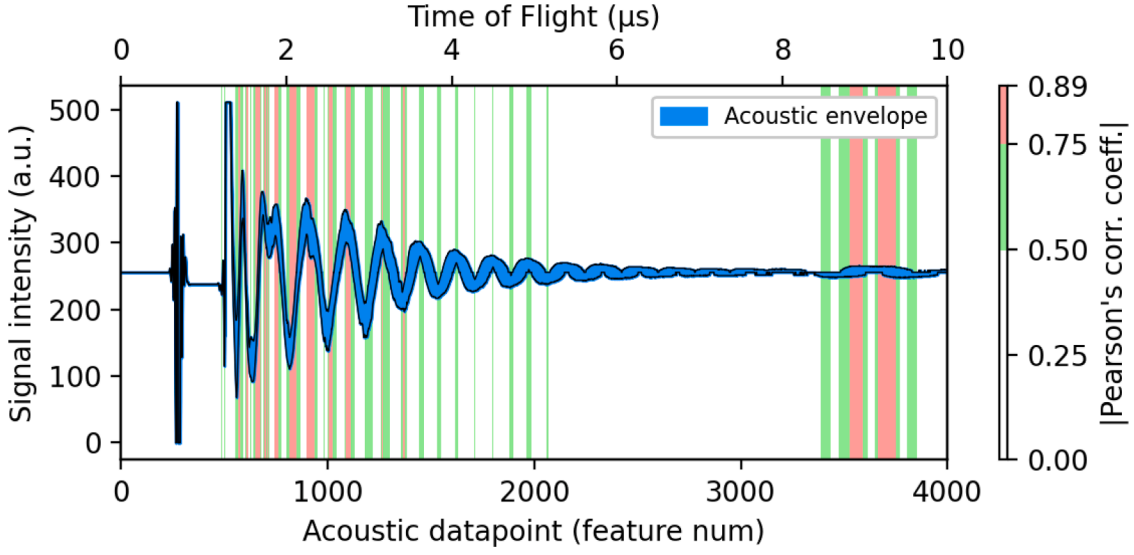

Fig. 3. Acoustic Envelope (time-domain) encapsulating all recorded waveforms. The Pearson correlation to the SoC colours the background for each acoustic datapoint.

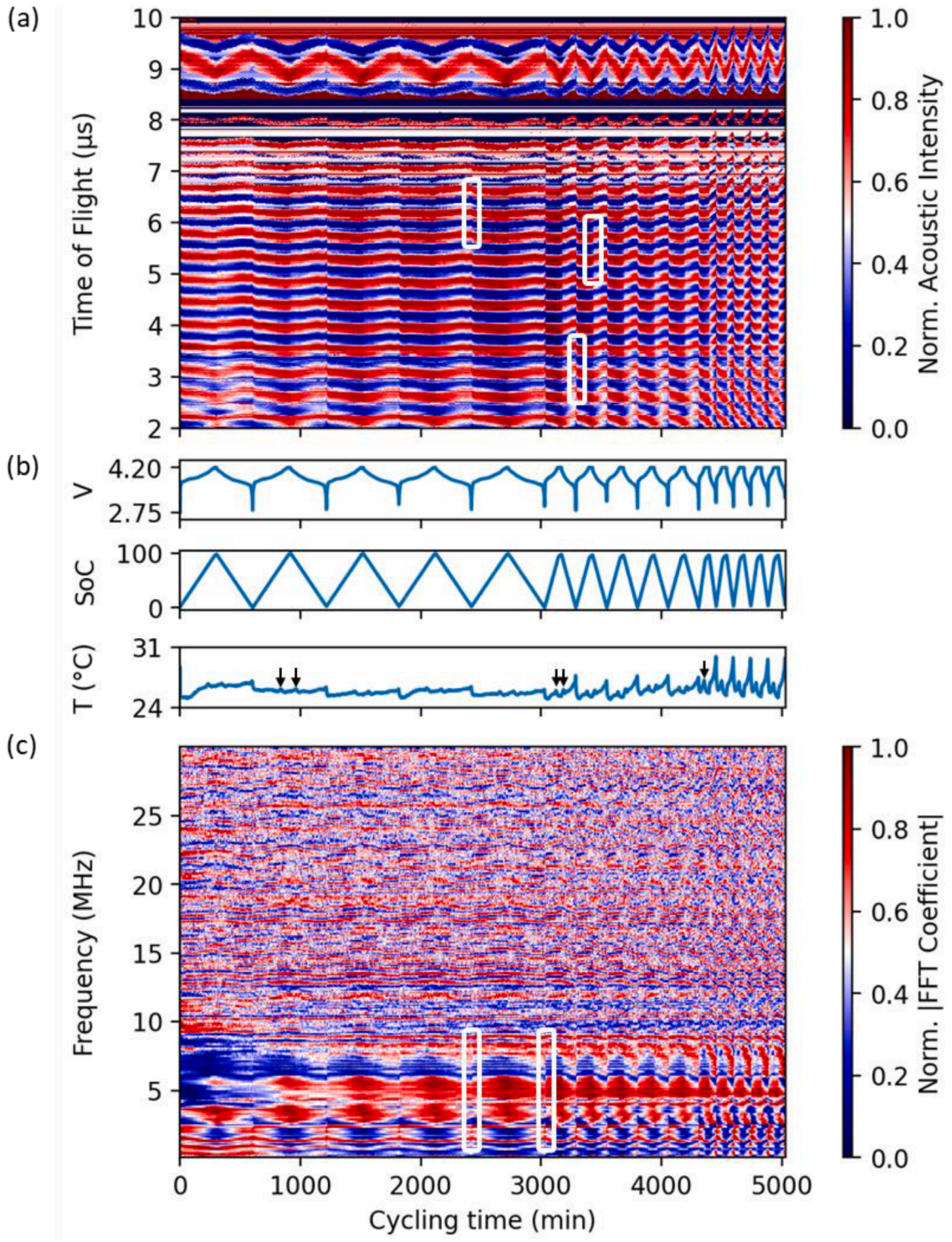

Fig. 4. Temporally resolved experimental data. Examples of abrupt acoustic transitions are shown circled. (a) Time-domain colour map with the first 2 µs cropped out as they contain invariable recordings of the actuation signal. (b) Voltage, SoC and temperature variations during the experiment. Five cycles at each of the rates C/5, C/2 and 1C can be distinguished based on their duration. Examples of temperature spikes at intermediate SoC are indicated by arrows. (c) Frequency-domain colourmap, showing the first 300 (out of 2000) frequencies.

which are temporally resolved representations of the acoustic dataset for the entire experiment. The periodicity of the acoustic intensity with cycling is clearly visible in the time-domain, while the frequency-domain depiction is more convoluted but patterns still emerge, especially at the lower frequencies. The normalisation performed is feature-wise, so that for any specific ToF in Fig. 4a the acoustic intensity attains values between 0 and 1. Similarly, for any specific frequency in Fig. 4c the Fourier coefficient magnitude was mapped to the 0–1 range. Animations A and B in the supplementary material provide a complementary view of acoustic variations with cycling in both the time and the frequency domains.

A feed-forward neural network (FFNN) was constructed to train and evaluate regression models using all data configurations. To our knowledge, this is the first implementation of deep learning to estimate

SoC using acoustic signatures. Work by other authors [55] used Support Vector Regression (SVR) with a short input vector, comprising only two acoustic features with the addition of cell voltage as a third feature in some cases. The training mechanism of SVR is to identify a subset the training points which are alone correlated to the target variable. These surviving points are called support vectors and can be efficiently identified via convex optimisation [70]. However, the number of support vectors generally increases with the size of the training set, resulting in models that can be cumbersome to evaluate. This can be the case when either the feature space considered is large, or the number of samples is large, or both. In contrast, FFNNs fix the functional form of the regression model prior to training, but allow the parameter values of its basis functions to be adapted during training. Although this optimisation is not convex, and is therefore slower during training, the resulting models can be significantly more compact and faster to evaluate than a SVR models with the same generalisation performance [71]. As the application of ultrasonic testing for SoC estimation is still a nascent technique, we postulate that a large dataset will be needed to capture its many sensitivities to factors such as the temperature, C-rate and transducer position. At the same time, extracting maximum information from each waveform will be required, likely leading to a large feature space. We propose the use of FFNNs with a range of data configurations as a scalable approach and demonstrate its feasibility using the aforementioned well-controlled dataset of CC-CV operation. Future work will evaluate the proposed workflow using bigger and more diverse data, including drive cycle operation which is also known to be observable using acoustics [69].

The FFNN architecture tested contains two hidden layers with 100 nodes each, and a single-node output layer yielding the SoC. Such structures, comprising more than one hidden layer, are often referred to as 'deep' [72]. The size of the input layer varied according to the input feature vector of each data configuration. Rectified linear activation functions were used in all hidden nodes. No activation was applied to the output node. Training was performed with a batch size of 128 samples, the mean absolute error was used as the loss function and training was allowed to proceed for 3000 epochs in all cases. During training, the learning rate was kept fixed at a value of 1×10^{-4} for the first 100 epochs and was then forced to decay linearly to a value of 2×10^{-5} in the remaining 2900 epochs. The regression model was constructed using the Sequential Model framework of the TensorFlow Keras Python library with the built-in 'Adam' optimiser.

Regardless of the data configuration, the available data pools were normalised and randomly sampled with an 80–20 split to produce training and test sets containing data obtained under different conditions. The variation of conditions primarily included the different cycling C-rates, but also the temperature which varied naturally in the absence of any temperature control. Each training and test set contained 4036 and 1009 signals respectively. To allow exploitation of the entire dataset for both training and testing, 5-fold stratified cross-validation was performed for each data configuration. Additionally, to show the progression and convergence of the training process, the 80% training data pool of each fold was used incrementally in five equal increments, while keeping the test set constant at 1009 signals. The performance of each data configuration was therefore evaluated with 25 separate regression models.

3. Results

It is worth noting the abrupt transitions in the acoustic characteristics of the cell which are visible on the colourmaps of Fig. 4. They are evident in the entirety of the time-domain representation and mostly at the lower frequencies of the frequency-domain. Similar observations in the time-domain are noted by Robinson et al. [50]. Colourmaps for individual C-rates are provided in supplementary Figures S2, S3 and S4, also highlighting these discontinuities. In all cases, abrupt transitions occur in sync with changes in the cycling protocol and are most evident where polarisation reversal occurs, especially at the bottom-of-discharge. At this point operation switches from discharging to charging, while the temperature spikes due to the entropic asymmetry of the charging and discharging processes [73] and the impedance of the LCO/graphite cell reaching a maximum [74,75]. This acoustic transition also becomes more pronounced at higher C-rates, accompanied by sharper temperature changes. The combination of electrochemically driven mechanical and thermal alterations in the cell at that point, and the added effect of the cycling rate, conceal the causality of the acoustic transition. Before further discussion it should be noted that the precise alignment of temperature peaks with the bottom-of-discharge indicates that there is no significant lag between bulk heat generation and temperature rise at the cell's surface, where measurements are taken.

The acoustic discontinuity at the top-of-charge is generally less pronounced and exhibits similar rate dependence with the bottom-of-discharge, appearing more subtle at lower C-rates. At C/5 no accompanying temperature response is observed at this point, therefore, the acoustic transition is due to stiffness changes alone, influenced by the reversal of electrochemical processes. At higher C-rates a local temperature minimum is observed at the top-of-charge, possibly influencing the acoustic response.

Temperature is known to have a very significant effect on the acoustic characteristics of battery cells over a broad range. Chang et al. [57] have demonstrated the temperature effect to be especially pronounced between acoustic measurements obtained 40–50°C apart, while Owen *et al.* [69] have explored this sensitivity over a 70°C window. Popp et al. [62] have shown temperature to have an identifiable influence on acoustics over a range smaller than 10°C. The lead-up to thermal runaway has also been found to strongly alter acoustic signatures, where temperature likely plays a role even if not in isolation [52]. Despite the above, the temperature variation in the data considered in this work is relatively modest, with a range of 5°C and a standard deviation of 0.6°C, as discussed. The effect of fluctuations of this magnitude on the acoustic characteristics is expected to be minimal. The absence of temperature sensitivity in relation to acoustic sampling over a similar temperature window is also noted by Robinson et al. [50].

In addition to the observed thermal effects at the top and bottom-of-charge, temperature peaks are also seen at intermediate SoCs, specifically at ca. 75% SoC during charge and ca. 87% SoC during discharge. Examples of these peaks are highlighted in Fig. 4 and Supplementary Figures S2-S4. They are attributed to thermodynamic characteristics of the cathode and anode at specific states of lithiation, resulting in reversible heating or cooling of entropic origin. Various calorimetry studies have investigated these effects, for whole $LiCoO_2$/graphite cells [76], half cells [77] or both [78,79]. Graphite anodes are known to restructure during lithiation, forming distinct metastable phases in a process known as staging [80]. Different stages have different thermodynamic footprints and could contribute to the temperature effects seen. However, at the SoC range of 75–87% considered, the thermal response is most likely dominated by the LCO cathode undergoing a brief hexagonal to monoclinic phase change [78,79]. In general, the heat generation rate from such reversible thermodynamic events is also known to scale in proportion to the applied current [73], resulting in amplification of the temperature spikes at higher rates as seen.

The acoustic response at these positions shows no discernible changes in the C/5 case (Supplementary Figure S2). When charging at C/2, patterns begin to emerge in the frequency domain, as highlighted in Supplementary Figure S3. These demonstrate the value that frequency-domain representations bring to acoustic battery examination. The same patterns appear more pronounced at 1C (Supplementary Figure S4), however, in this case they also coincide with the onset of the constant voltage step and associated cell relaxation. The minor acoustic shift seen during C/2 testing is free of C-rate effects, yet it cannot be conclusively attributed to the temperature change alone either. It must also be considered that transformations in the cathode and anode can also alter the stiffness characteristics of the cell. Tavassol et al. [81] have

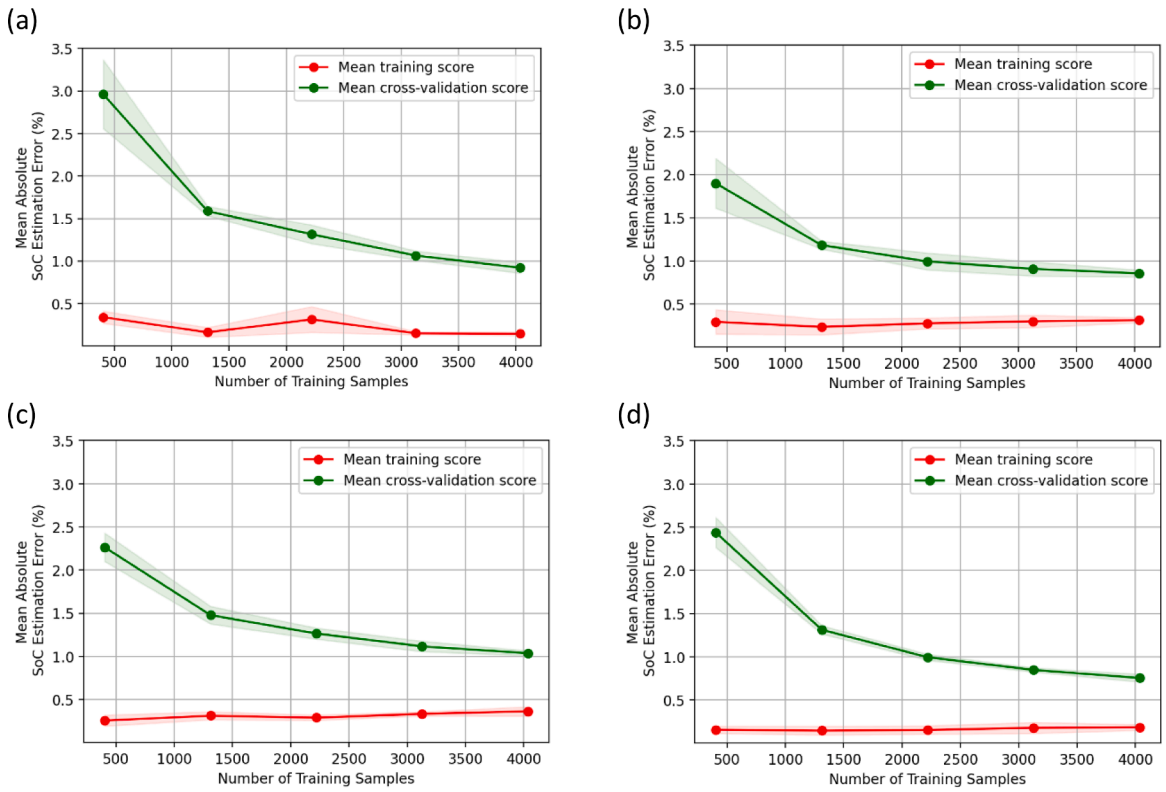

Fig. 5. 5-fold cross-validated learning curves of the tested data configurations. (a) 4000 features (time-domain), (b) 995 features (time-domain), (c) 361 features (time-domain), (d) 300 features (frequency-domain).

demonstrated experimentally that the formation of intercalation compounds can result in rapid stress-strain developments, while Qi et al. [82] have shown through Density Functional Theory simulations that the polycrystalline Young's moduli of different graphite stages differ notably.

It is worth noting that as the cell temperature is strongly dependant on the cycling rate, separating the acoustic effects of the two requires the temperature to be treated as an additional feature dimension, and additional datasets are needed to provide reasonable coverage of the SoC-temperature plane. The dependence of cell stiffness on the electrochemical potential, SoC and kinetics, captured by the term 'electrochemical stiffness' [50,81] must also be considered. In this work, however, we focus on determining whether the trained models are able to produce accurate SoC estimates using the acoustic signatures alone, despite the presence of these phenomena.

The performance of the FFNN regression model, when trained and tested using the four data configurations listed in Table 1, is shown in Figs. 5a-d. Each figure takes the form of a cross-validated learning curve with point marks representing the average of a five-fold evaluation and the shaded regions showing the respective standard deviation. It is observed, in all cases, that the expansion of the training dataset to include more samples improves the average cross-validated accuracy of the estimation. This is testament to the method's flexibility to produce reasonable estimates even with small amounts of data, and to its predictive potential in the presence of larger data pools. The consistency of the prediction is also seen to generally improve with increasing amounts of training data, evidenced by a decrease in the standard deviation of the cross-validation error. The performance of the model on the training set is also plotted as evidence that a healthy separation of the training and test sets has taken place, and that the applied training routine has prevented overfitting to the training set. The presence of a gap between the cross-validation and training learning curves and their near-asymptotic approach are suggestive of the above.

In comparison to the data configuration using all 4000 time-domain features (Fig. 5a), the data configurations that employ feature filtering based on the Pearson correlation coefficient (Figs. 5b-c) perform similarly or even better across all training pool sizes. Mean-absolute errors in the vicinity of 1% are achieved in these cases. When the maximum amount of training samples is utilised, moderate filtering (data configuration 2) marginally outperforms the unfiltered case, while high filtering (data configuration 3) marginally underperforms it. It is not surprising that providing higher quality filtered features to the neural network can allow higher accuracy levels to be reached under the same training process and network architecture. However, it should be noted that as the Pearson implementation is a measure of the linear correlation between acoustic features and the SoC, its use for filtering may not always translate into better predictions. It is reasonable to assume that acoustic datasets with much greater levels of non-linearity are possible, when different cell chemistries, geometries and operating conditions are considered. It is in such cases that the use of an unfiltered data configuration could be most valuable, allowing all sensitivities to emerge through the training process.

The frequency-domain configuration was found to be the best-performing in our tests, yielding the most accurate estimates at large training pool sizes and achieving an accuracy of approximately 0.75% SoC. Although the frequency-domain has a visually more convoluted appearance than the time-domain in Fig. 4, it is found to yield features that correlate more strongly with SoC than their time-domain counterparts and has a higher predictive value. The frequency-domain configuration also contains the smallest number of features in our study, with associated benefits of computational economy since the added computational overhead of the FFT algorithm is minimal.

The performance of the model using the frequency-domain configuration is discussed in more detail henceforth. Because the acoustic acquisition frequency was kept constant throughout the experiment, our dataset contains more acoustic signatures for the slower rates which took longer to complete (Fig. 8). This inherent bias was propagated into the training and test sets as those were produced by random sampling.

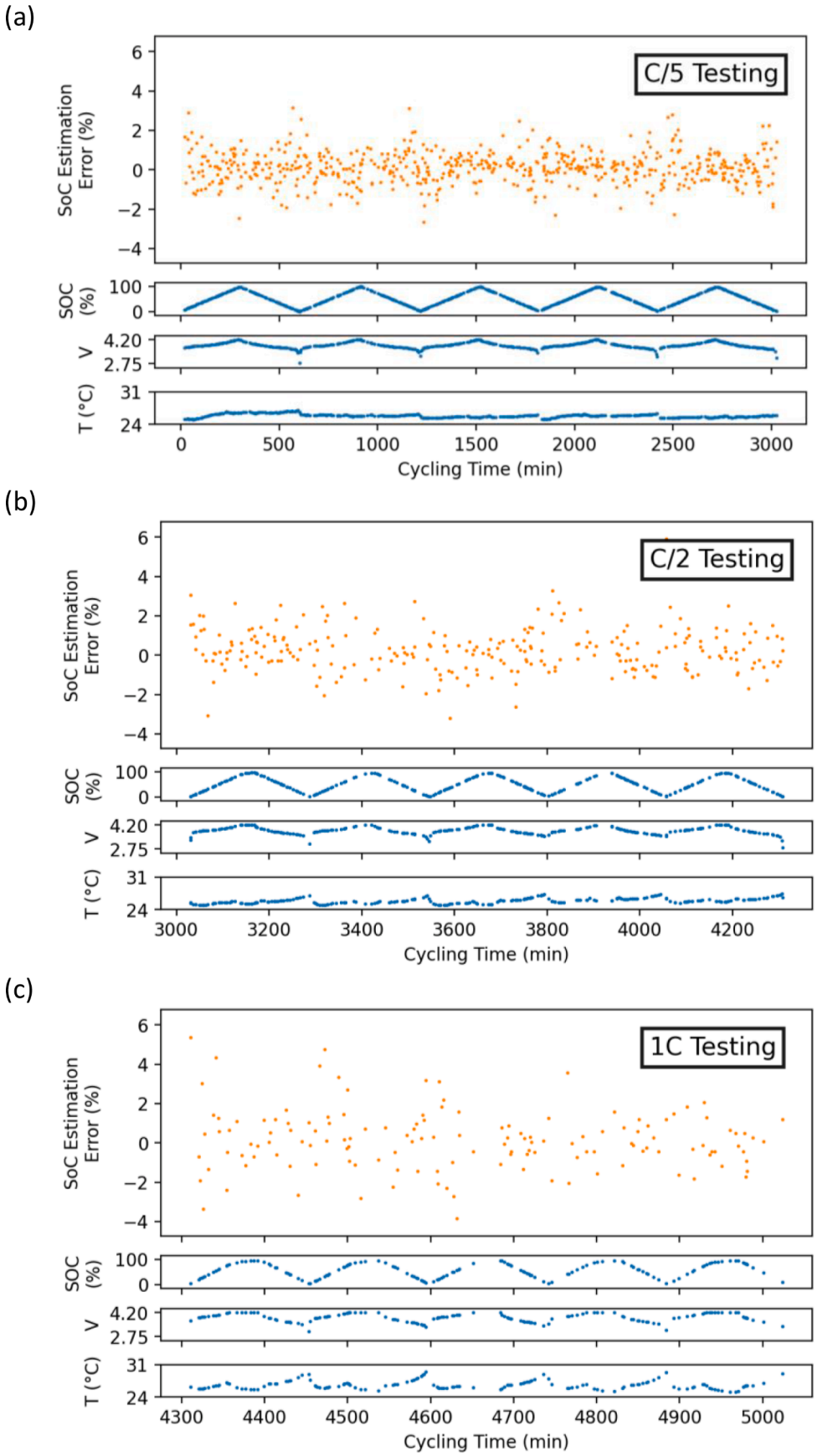

Fig. 6. Regression model error per test data point for the frequency-domain configuration. Orange colour shows the SoC estimation error. Blue colour indicates complementary information about the test data. (a) C/5 test data, (b) C/2 test data, (c) 1C test data.

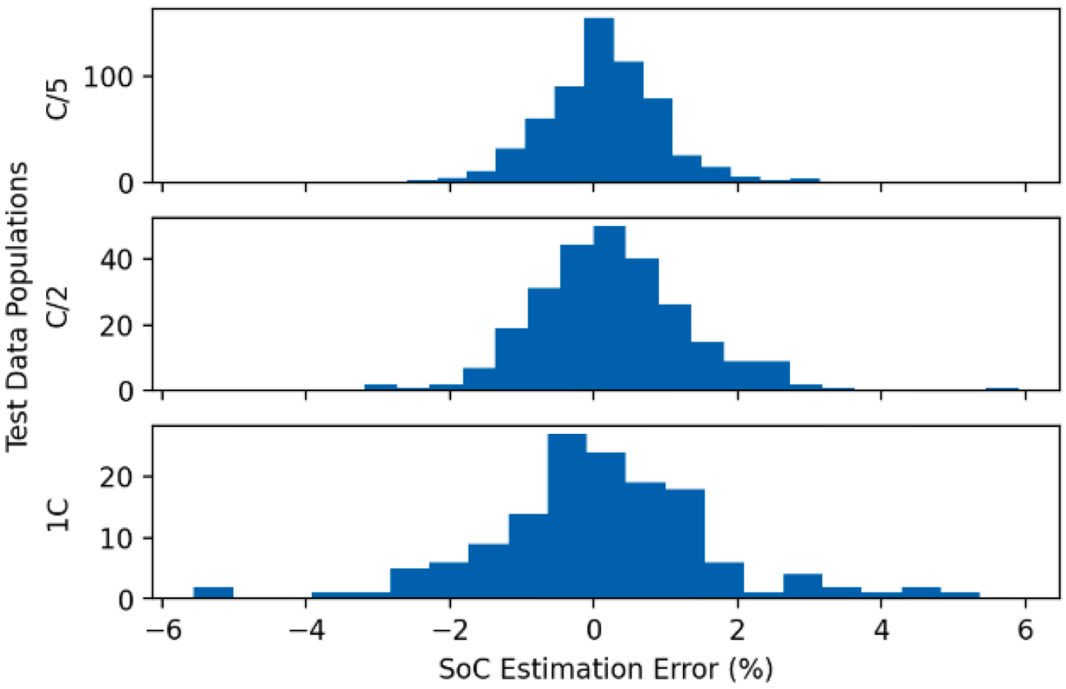

Fig. 7. SoC estimation error histograms per C-rate. Results from model based on the frequency-domain configuration.

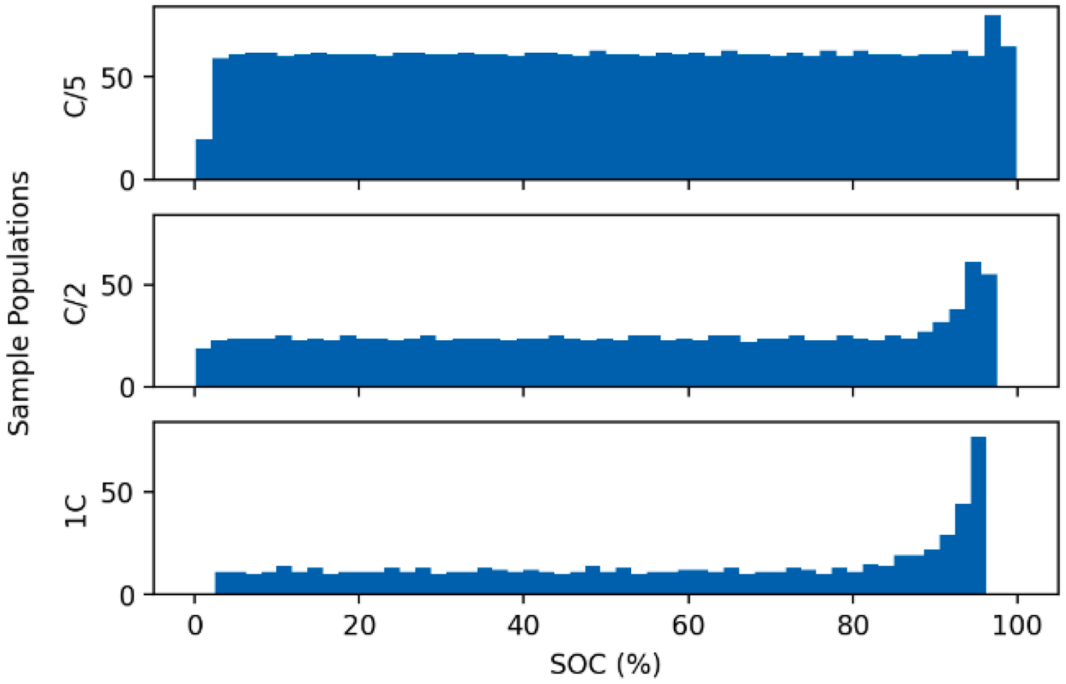

Fig. 8. Acoustic sample populations in the entire dataset, per SoC and C-rate.

Figs. 6a-c show the performance of the regression model by C-rate, when trained and tested on frequency-domain data. It is shown that increasing data scarcity results in increasing estimation errors in the higher C-rate cases. This is an expected pattern, as it has already been established that increasing amounts of data provide a net accuracy benefit and that there is no evidence of sustained data saturation in the modelling.

We hesitate to draw conclusions about the accuracy of the model at different SoC bands, or about the influence that temperature has on the model's estimation error. We do, however, speculate that the SoC estimation error at the bottom-of-discharge shows a greater spread compared to the top of charge. In one respect, inference at the SoC extremities may suffer from proximity to the edges of the data range, introducing an element of extrapolation to the computation. At the top-of-charge this is likely counteracted by the availability of more data points, due to the slower constant voltage regime having allowed the collection of more acoustic samples.

A complementary view of the estimation error per C-rate is given in Fig. 7. Together with the population histograms of Fig. 8, the link between accuracy and data abundance is again clear. While temperature variability in the collected dataset has been limited, it is a likely

contributor to the reduced estimation accuracy seen at higher C-rates, together with the rate-dependence of the electrochemical stiffness. Given additional data coverage, it is expected that the proposed method will be capable of learning such dependencies during the training process, and that it will achieve to differentiate features that correlate to SoC across cases. The diminished accuracy in the 1C estimates, which is in the region of 1.2%, is still largely adequate for practical implementations of the method. The accuracy under the C/5 regime is approximately 0.6%, which can be superior to electrochemical and other alternative SoC estimation techniques. The average accuracy for the entire dataset, using the frequency configuration, is ca. 0.75% as discussed. It is worth reiterating that the proposed method is independent of voltage or temperature measurements, making it suitable for applications where redundancy and diversity of SoC estimators is valued.

4. Conclusions

Acoustic signatures obtained experimentally from a 210 mAh LCO pouch cell under CC-CV cycling have been utilised to perform SoC inference using a feed-forward neural network regression model. Four data configurations were considered. (1) Entire signal waveforms; (2)-(3) selected waveform features based on thresholds on their Pearson correlation to SoC; (4) Fourier coefficient magnitudes of the 15% lowest frequencies. It is demonstrated that a FFNN of modest size can be trained using acoustic waveforms in their entirety, avoiding the need for any feature selection to take place. Mean absolute estimation errors in the vicinity of 1% were achieved with this approach, showing its potential for deployment in streamlined workflows. SoC estimates produced by the filtered data configurations are of comparable accuracy, while using reduced input vectors of time-domain features selected based on statistical significance. These provide an efficient, formal and robust solution of dimensionality reduction, for applications where computational economy is prioritised. The highest accuracy is achieved using the frequency-domain configuration, with a mean absolute error of 0.75%. FFT appears to have a positive filtering or amplification effect on the dataset, yielding features that correlate most highly with the SoC. Importantly, the high accuracy of all data configurations is accomplished using acoustic information alone, without assistive voltage or temperature measurements. This demonstrates the potential of the acoustic method to be deployed as an independent SoC estimation technique in operando, with direct safety and reliability benefits. Additional applications arise, including the online validation of voltage-SoC mappings by comparison to acoustic SoC estimates, and the fault-detection of the respective voltage sensors. In the continuation of this work, the proposed method will be evaluated on data pools of multiple cells, where greater variations in the operating temperature and inherent electrochemical stiffness will be an additional challenge. In this, a machine learning approach using FFNNs is expected to be most powerful.

Declaration of Competing Interests

The authors declare that they have no known competing financial interests or personal relationships that could have appeared to influence the work reported in this paper.

Acknowledgements

The authors acknowledge funding and support from the Faraday Institution (EP/S003053/1) as part of the Multi-Scale Modelling (FIRG025) and LiSTAR (FIRG014) projects. The Royal Academy of Engineering is acknowledged for the financial support of Shearing (CiET1718\59) and Brett under the Research Chairs and Senior Research Fellowships scheme (RCSRF2021/13/53). Galiounas acknowledges The Alan Turing Institute for the provision of training and computational resources.

Supplementary materials

Supplementary material associated with this article can be found, in the online version, at doi:10.1016/j.egyai.2022.100188.

References

[1] Hannan MA, Lipu MSH, Hussain A, Mohamed A. A review of lithium-ion battery state of charge estimation and management system in electric vehicle applications: challenges and recommendations. Renew Sustain Energy Rev Oct. 2017;78:834–54. https://doi.org/10.1016/J.RSER.2017.05.001.
[2] Xiong R, Cao J, Yu Q, He H, Sun F. Critical Review on the Battery State of Charge Estimation Methods for Electric Vehicles. IEEE Access 2018;6:1832–43. https://doi.org/10.1109/ACCESS.2017.2780258.
[3] How DNT, Hannan MA, Hossain Lipu MS, Ker PJ. State of Charge Estimation for Lithium-Ion Batteries Using Model-Based and Data-Driven Methods: a Review. IEEE Access 2019;7:136116–36. https://doi.org/10.1109/ACCESS.2019.2942213.
[4] Liu Y, He Y, Bian H, Guo W, Zhang X. A review of lithium-ion battery state of charge estimation based on deep learning: directions for improvement and future trends. J Energy Storage 2022;52:104664. https://doi.org/10.1016/j.est.2022.104664.
[5] Jeong Y-M, Cho Y-K, Ahn J-H, Ryu S-H, Lee B-K. Enhanced Coulomb counting method with adaptive SOC reset time for estimating OCV. In: 2014 IEEE Energy Conversion Congress and Exposition (ECCE); 2014. p. 1313–8. https://doi.org/10.1109/ECCE.2014.6953989.
[6] Cheng KWE, Divakar BP, Wu H, Ding K, Ho HF. Battery-management system (BMS) and SOC development for electrical vehicles. IEEE Trans Veh Technol 2010;60(1):76–88.
[7] Xing Y, He W, Pecht M, Tsui KL. State of charge estimation of lithium-ion batteries using the open-circuit voltage at various ambient temperatures. Appl Energy 2014;113:106–15. https://doi.org/10.1016/j.apenergy.2013.07.008.
[8] Pattipati B, Balasingam B, Avvari GV, Pattipati KR, Bar-Shalom Y. Open circuit voltage characterization of lithium-ion batteries. J Power Sources 2014;269:317–33. https://doi.org/10.1016/j.jpowsour.2014.06.152.
[9] Zhang R, et al. A Study on the Open Circuit Voltage and State of Charge Characterization of High Capacity Lithium-Ion Battery Under Different Temperature. Energies 2018;11(9). https://doi.org/10.3390/en11092408.
[10] Yu Q-Q, Xiong R, Wang L-Y, Lin C. A Comparative Study on Open Circuit Voltage Models for Lithium-ion Batteries. Chinese J Mech Eng 2018;31(1):65. https://doi.org/10.1186/s10033-018-0268-8.
[11] Zhang T, Marinescu M, O'Neill L, Wild M, Offer G. Modeling the voltage loss mechanisms in lithium–sulfur cells: the importance of electrolyte resistance and precipitation kinetics. Phys Chem Chem Phys 2015;17(35):22581–6.
[12] Chen C-H, Brosa Planella F, O'Regan K, Gastol D, Widanage WD, Kendrick E. Development of Experimental Techniques for Parameterization of Multi-scale Lithium-ion Battery Models. J Electrochem Soc May 2020;167(8):080534. https://doi.org/10.1149/1945-7111/ab9050.
[13] Wang A, et al. Review of parameterisation and a novel database (LiionDB) for continuum Li-ion battery models. Prog Energy 2022.
[14] Nejad S, Gladwin DT, Stone DA. A systematic review of lumped-parameter equivalent circuit models for real-time estimation of lithium-ion battery states. J Power Sources 2016;316:183–96. https://doi.org/10.1016/j.jpowsour.2016.03.042.
[15] Plett GL. Equivalent-Circuit Models," in *Battery management systems*. battery modeling 2015;Volume 1:29–63.
[16] Xu J, Mi CC, Cao B, Cao J. A new method to estimate the state of charge of lithium-ion batteries based on the battery impedance model. J Power Sources 2013;233:277–84. https://doi.org/10.1016/j.jpowsour.2013.01.094.
[17] Ciucci F. Modeling electrochemical impedance spectroscopy. Curr Opin Electrochem 2019;13:132–9. https://doi.org/10.1016/j.coelec.2018.12.003.
[18] Cui Z, Wang L, Li Q, Wang K. A comprehensive review on the state of charge estimation for lithium-ion battery based on neural network. Int J Energy Res 2022;46(5):5423–40. https://doi.org/10.1002/er.7545.
[19] Vidal C, Malysz P, Kollmeyer P, Emadi A. Machine Learning Applied to Electrified Vehicle Battery State of Charge and State of Health Estimation: state-of-the-Art. IEEE Access 2020;8:52796–814. https://doi.org/10.1109/ACCESS.2020.2980961.
[20] Kim T, Qiao W, Qu L. An Enhanced Hybrid Battery Model. IEEE Trans Energy Convers 2019;34(4):1848–58. https://doi.org/10.1109/TEC.2019.2935700.
[21] Yang X, Chen Y, Li B, Luo D. Battery states online estimation based on exponential decay particle swarm optimization and proportional-integral observer with a hybrid battery model. Energy 2020;191:116509. https://doi.org/10.1016/j.energy.2019.116509.
[22] Plett GL. Extended Kalman filtering for battery management systems of LiPB-based HEV battery packs - Part 1. Background. J Power Sources Aug. 2004;134(2):252–61. https://doi.org/10.1016/j.jpowsour.2004.02.031.
[23] Plett GL. Extended Kalman filtering for battery management systems of LiPB-based HEV battery packs - Part 2. Modeling and identification. J Power Sources Aug. 2004;134(2):262–76. https://doi.org/10.1016/j.jpowsour.2004.02.032.
[24] Plett GL. Extended Kalman filtering for battery management systems of LiPB-based HEV battery packs - Part 3. State and parameter estimation. J Power Sources Aug. 2004;134(2):277–92. https://doi.org/10.1016/j.jpowsour.2004.02.033.

[25] Di Domenico D, Stefanopoulou A, Fiengo G. Lithium-Ion Battery State of Charge and Critical Surface Charge Estimation Using an Electrochemical Model-Based Extended Kalman Filter. J Dyn Syst Meas Control Oct. 2010;132(6). https://doi.org/10.1115/1.4002475.

[26] Xiong R, He H, Sun F, Zhao K. Evaluation on State of Charge Estimation of Batteries With Adaptive Extended Kalman Filter by Experiment Approach. IEEE Trans Veh Technol 2013;62(1):108–17. https://doi.org/10.1109/TVT.2012.2222684.

[27] Liu C, Liu W, Wang L, Hu G, Ma L, Ren B. A new method of modeling and state of charge estimation of the battery. J Power Sources 2016;320:1–12. https://doi.org/10.1016/j.jpowsour.2016.03.112.

[28] He W, Williard N, Chen C, Pecht M. State of charge estimation for electric vehicle batteries using unscented kalman filtering. Microelectron Reliab 2013;53(6):840–7. https://doi.org/10.1016/j.microrel.2012.11.010.

[29] Li J, Barillas JKlee, Guenther C, Danzer MA. A comparative study of state of charge estimation algorithms for LiFePO4 batteries used in electric vehicles. J Power Sources 2013;230:244–50. https://doi.org/10.1016/j.jpowsour.2012.12.057.

[30] He Z, et al. State-of-charge estimation of lithium ion batteries based on adaptive iterative extended Kalman filter. J Energy Storage 2021;39:102593. https://doi.org/10.1016/j.est.2021.102593.

[31] Charkhgard M, Farrokhi M. State-of-Charge Estimation for Lithium-Ion Batteries Using Neural Networks and EKF. IEEE Trans Ind Electron 2010;57(12):4178–87. https://doi.org/10.1109/TIE.2010.2043035.

[32] He W, Williard N, Chen C, Pecht M. State of charge estimation for Li-ion batteries using neural network modeling and unscented Kalman filter-based error cancellation. Int J Electr Power Energy Syst 2014;62:783–91. https://doi.org/10.1016/j.ijepes.2014.04.059.

[33] How DNT, Hannan MA, Lipu MSH, Sahari KSM, Ker PJ, Muttaqi KM. State-of-Charge Estimation of Li-ion Battery in Electric Vehicles: a Deep Neural Network Approach. In: 2019 IEEE Industry Applications Society Annual Meeting; 2019. p. 1–8. https://doi.org/10.1109/IAS.2019.8912003.

[34] Guo Y, Yang Z, Liu K, Zhang Y, Feng W. A compact and optimized neural network approach for battery state-of-charge estimation of energy storage system. Energy 2021;219:119529. https://doi.org/10.1016/j.energy.2020.119529.

[35] Bhattacharjee A, Verma A, Mishra S, Saha TK. Estimating State of Charge for xEV Batteries Using 1D Convolutional Neural Networks and Transfer Learning. IEEE Trans Veh Technol 2021;70(4):3123–35. https://doi.org/10.1109/TVT.2021.3064287.

[36] Vidal C, Kollmeyer P, Chemali E, Emadi A. Li-ion Battery State of Charge Estimation Using Long Short-Term Memory Recurrent Neural Network with Transfer Learning. In: 2019 IEEE Transportation Electrification Conference and Expo (ITEC); 2019. p. 1–6. https://doi.org/10.1109/ITEC.2019.8790543.

[37] Hannan MA, et al. Toward Enhanced State of Charge Estimation of Lithium-ion Batteries Using Optimized Machine Learning Techniques. Sci Rep 2020;10(1):4687. https://doi.org/10.1038/s41598-020-61464-7.

[38] Chen J, Feng X, Jiang L, Zhu Q. State of charge estimation of lithium-ion battery using denoising autoencoder and gated recurrent unit recurrent neural network. Energy 2021;227:120451. https://doi.org/10.1016/j.energy.2021.120451.

[39] Feng X, Chen J, Zhang Z, Miao S, Zhu Q. State-of-charge estimation of lithium-ion battery based on clockwork recurrent neural network. Energy 2021;236:121360. https://doi.org/10.1016/j.energy.2021.121360.

[40] Wang S, Takyi-Aninakwa P, Jin S, Yu C, Fernandez C, Stroe D-I. An improved feedforward-long short-term memory modeling method for the whole-life-cycle state of charge prediction of lithium-ion batteries considering current-voltage-temperature variation. Energy 2022;254:124224. https://doi.org/10.1016/j.energy.2022.124224.

[41] Majasan JO, et al. Recent advances in acoustic diagnostics for electrochemical power systems. J Phys Energy Jun. 2021;3(3):032011. https://doi.org/10.1088/2515-7655/ABFB4A.

[42] Betta G, Daponte P. Detection of Echoes in Noisy Environments for Multilayer Structure Characterization. IEEE Trans Instrum Meas 1993;42(4):834–41. https://doi.org/10.1109/19.234494.

[43] Daponte P, Fazio G, Molinaro A. Detection of echoes using time-frequency analysis techniques. IEEE Trans Instrum Meas Feb. 1996;45(1):30–40. https://doi.org/10.1109/19.481308.

[44] Angrisani L, Daponte P, D'Apuzzo M. The detection of echoes from multilayer structures using the wavelet transform. IEEE Trans Instrum Meas Aug. 2000;49(4):727–31. https://doi.org/10.1109/19.863914.

[45] Grimaldi D. Time-of-flight measurement of ultrasonic pulse echoes using wavelet networks. IEEE Trans Instrum Meas Feb. 2006;55(1):5–13. https://doi.org/10.1109/TIM.2005.862021.

[46] Wang Z, Huang S, Wang S, Wang Q, Zhao W. A Damage Localization Method with Multimodal Lamb Wave Based on Adaptive Polynomial Chirplet Transform. IEEE Trans Instrum Meas Oct. 2020;69(10):8076–87. https://doi.org/10.1109/TIM.2020.2993342.

[47] Ladpli P, Kopsaftopoulos F, Chang FK. Estimating state of charge and health of lithium-ion batteries with guided waves using built-in piezoelectric sensors/actuators. J Power Sources Apr. 2018;384:342–54. https://doi.org/10.1016/J.JPOWSOUR.2018.02.056.

[48] Copley RJ, Cumming D, Wu Y, Dwyer-Joyce RS. Measurements and modelling of the response of an ultrasonic pulse to a lithium-ion battery as a precursor for state of charge estimation. J Energy Storage Apr. 2021;36:102406. https://doi.org/10.1016/J.EST.2021.102406.

[49] Ladpli P, Liu C, Kopsaftopoulos F, Chang FK. Estimating Lithium-ion Battery State of Charge and Health with Ultrasonic Guided Waves Using an Efficient Matching Pursuit Technique. In: ITEC Asia-Pacific 2018 - 2018 IEEE Transp. Electrif. Conf. Expo, Asia-Pacific E-Mobility A Journey from Now Beyond; Aug. 2018. https://doi.org/10.1109/ITEC-AP.2018.8433297.

[50] Robinson JB, Pham M, Kok MDR, Heenan TMM, Brett DJL, Shearing PR. Examining the Cycling Behaviour of Li-Ion Batteries Using Ultrasonic Time-of-Flight Measurements. J Power Sources Dec. 2019;444:227318. https://doi.org/10.1016/J.JPOWSOUR.2019.227318.

[51] Knehr KW, Hodson T, Bommier C, Davies G, Kim A, Steingart DA. Understanding Full-Cell Evolution and Non-chemical Electrode Crosstalk of Li-Ion Batteries. Joule Jun. 2018;2(6):1146–59. https://doi.org/10.1016/J.JOULE.2018.03.016.

[52] Pham MTM, et al. Correlative acoustic time-of-flight spectroscopy and X-ray imaging to investigate gas-induced delamination in lithium-ion pouch cells during thermal runaway. J Power Sources Sep. 2020;470:228039. https://doi.org/10.1016/J.JPOWSOUR.2020.228039.

[53] Gold L, et al. Probing lithium-ion batteries' state-of-charge using ultrasonic transmission – Concept and laboratory testing. J Power Sources Mar. 2017;343:536–44. https://doi.org/10.1016/J.JPOWSOUR.2017.01.090.

[54] Robinson JB, et al. Identifying Defects in Li-Ion Cells Using Ultrasound Acoustic Measurements. J Electrochem Soc Sep. 2020;167(12):120530. https://doi.org/10.1149/1945-7111/ABB174.

[55] Davies G, et al. State of Charge and State of Health Estimation Using Electrochemical Acoustic Time of Flight Analysis. J Electrochem Soc Sep. 2017;164(12):A2746. https://doi.org/10.1149/2.1411712JES.

[56] Bommier C, et al. In Operando Acoustic Detection of Lithium Metal Plating in Commercial LiCoO2/Graphite Pouch Cells. Cell Reports Phys Sci Apr. 2020;1(4):100035. https://doi.org/10.1016/J.XCRP.2020.100035.

[57] Chang W, Bommier C, Fair T, Yeung J, Patil S, Steingart D. Understanding Adverse Effects of Temperature Shifts on Li-Ion Batteries: an Operando Acoustic Study. J Electrochem Soc Feb. 2020;167(9):090503. https://doi.org/10.1149/1945-7111/AB6C56.

[58] Chang W, Steingart D. Operando 2D Acoustic Characterization of Lithium-Ion Battery Spatial Dynamics. ACS Energy Lett Jul. 2021;6:2960–8. https://doi.org/10.1021/ACSENERGYLETT.1C01324.

[59] Chang W, et al. Measuring effective stiffness of Li-ion batteries via acoustic signal processing. J Mater Chem A Aug. 2020;8(32):16624–35. https://doi.org/10.1039/D0TA05552B.

[60] Hsieh AG, et al. Electrochemical-acoustic time of flight: in operando correlation of physical dynamics with battery charge and health. Energy Environ Sci May 2015;8(5):1569–77. https://doi.org/10.1039/C5EE00111K.

[61] Sood B, Osterman M, Pecht M. Health monitoring of lithium-ion batteries. In: Proc. - 10th Annu. IEEE Symp. Prod. Compliance Eng. ISPCE 2013; 2013. https://doi.org/10.1109/ISPCE.2013.6664165.

[62] Popp H, Koller M, Keller S, Glanz G, Klambauer R, Bergmann A. State Estimation Approach of Lithium-Ion Batteries by Simplified Ultrasonic Time-of-Flight Measurement. IEEE Access 2019;7:170992–1000. https://doi.org/10.1109/ACCESS.2019.2955556.

[63] Koyama Y, Chin TE, Rhyner U, Holman RK, Hall SR, Chiang YM. Harnessing the Actuation Potential of Solid-State Intercalation Compounds. Adv Funct Mater Mar. 2006;16(4):492–8. https://doi.org/10.1002/ADFM.200500633.

[64] Michael H, Jervis R, Brett DJL, Shearing PR. Developments in Dilatometry for Characterisation of Electrochemical Devices. Batter Supercaps Sep. 2021;4(9):1378–96. https://doi.org/10.1002/BATT.202100027.

[65] Robinson JB, Maier M, Alster G, Compton T, Brett DJL, Shearing PR. Spatially resolved ultrasound diagnostics of Li-ion battery electrodes. Phys Chem Chem Phys Mar. 2019;21(12):6354–61. https://doi.org/10.1039/C8CP07098A.

[66] Biot MA. Theory of Propagation of Elastic Waves in a Fluid-Saturated Porous Solid. I. Low-Frequency Range. J Acoust Soc Am 1956;28(2):168–78. https://doi.org/10.1121/1.1908239.

[67] Biot MA. Theory of Propagation of Elastic Waves in a Fluid-Saturated Porous Solid. II. Higher Frequency Range. J Acoust Soc Am 1956;28(2):179–91. https://doi.org/10.1121/1.1908241.

[68] Mallat SG, Zhang Z. Matching Pursuits With Time-Frequency Dictionaries. IEEE Trans Signal Process 1993;41(12):3397–415. https://doi.org/10.1109/78.258082.

[69] Owen RE, et al. Operando Ultrasonic Monitoring of Lithium-Ion Battery Temperature and Behaviour at Different Cycling Rates and under Drive Cycle Conditions. J Electrochem Soc Apr. 2022;169(4):40563. https://doi.org/10.1149/1945-7111/ac6833.

[70] Murphy KP. Probabilistic machine learning : an introduction. Cambridge: MIT Press; 2022.

[71] Bishop CM. Pattern recognition and machine learning. New York: Springer; 2006.

[72] Goodfellow I, Bengio Y, Courville A. Deep learning. MIT Press; 2016.

[73] Heubner C, Schneider M, Michaelis A. Detailed study of heat generation in porous LiCoO2 electrodes. J Power Sources Mar. 2016;307:199–207. https://doi.org/10.1016/J.JPOWSOUR.2015.12.096.

[74] Erol S, Orazem ME, Muller RP. Influence of overcharge and over-discharge on the impedance response of LiCoO2|C batteries. J Power Sources Dec. 2014;270:92–100. https://doi.org/10.1016/J.JPOWSOUR.2014.07.038.

[75] Zhang SS, Xu K, Jow TR. Charge and discharge characteristics of a commercial LiCoO2-based 18650 Li-ion battery. J Power Sources Oct. 2006;160(2):1403–9. https://doi.org/10.1016/J.JPOWSOUR.2006.03.037.

[76] Saito Y, Takano K, Kanari K, Negishi A, Nozaki K, Kato K. Comparative study of thermal behaviors of various lithium-ion cells. J Power Sources Jul. 2001;97–98:688–92. https://doi.org/10.1016/S0378-7753(01)00702-9.

[77] Lu W, Prakash J. In Situ Measurements of Heat Generation in a Li/Mesocarbon Microbead Half-Cell. J Electrochem Soc Mar. 2003;150(3):A262–6. https://doi.org/10.1149/1.1541672/XML.

[78] Al Hallaj S, Venkatachalapathy R, Prakash J, Selman JR. Entropy Changes Due to Structural Transformation in the Graphite Anode and Phase Change of the LiCoO [sub 2] Cathode. J Electrochem Soc Jul. 2000;147(7):2432. https://doi.org/10.1149/1.1393549/XML.

[79] Kobayashi Y, Miyashiro H, Kumai K, Takei K, Iwahori T, Uchida I. Precise Electrochemical Calorimetry of LiCoO2/Graphite Lithium-Ion Cell : understanding Thermal Behavior and Estimation of Degradation Mechanism. J Electrochem Soc Jun. 2002;149(8):A978. https://doi.org/10.1149/1.1487833.

[80] Sethuraman VA, Hardwick LJ, Srinivasan V, Kostecki R. Surface structural disordering in graphite upon lithium intercalation/deintercalation. J Power Sources Jun. 2010;195(11):3655–60. https://doi.org/10.1016/J.JPOWSOUR.2009.12.034.

[81] Tavassol H, Jones EMC, Sottos NR, Gewirth AA. Electrochemical stiffness in lithium-ion batteries. Nat Mater Aug. 2016;15(11):1182–7. https://doi.org/10.1038/nmat4708. 2016 1511.

[82] Qi Y, Guo H, Hector LG, Timmons A. Threefold Increase in the Young's Modulus of Graphite Negative Electrode during Lithium Intercalation. J Electrochem Soc Mar. 2010;157(5):A558. https://doi.org/10.1149/1.3327913/XML.